

Research Article

Earthquake Source Parameters of Moderate to Small Earthquake and Scaling Relationships in the Western Himalaya: Seismic Hazard Implication

Vedprakash Thakur¹ , Sanjay Kumar Prajapati^{1,*} , Birendra Pratap²,
Uma Shankar², Sudipto Bhattacharjee¹

¹National Center for Seismology, Ministry of Earth Sciences, New Delhi, India

²Department of Geophysics, Faculty of Sciences, Banaras Hindu University, Varanasi, India

Abstract

The Northwest Himalayas experiences frequent seismic activity, with numerous moderate events occurring over the past century, leading to several disasters. In the present study, we conducted a comprehensive analysis of the source parameters for 125 earthquakes with local magnitudes (ML) ≥ 4.0 that occurred in the northwest region during the period from 2013 to 2019. We analyzed the P and S wave spectra using Brune's source model to investigate the self-relation and self-similarity of earthquakes in the area. The digital seismograms used in this study were recorded by sixteen permanent broad-band stations at hypocentral distances between 10 and 327 km. The average ratio of P/S wave corner frequency is found in the range of 1.1-1.9, suggesting a higher corner frequency for the P wave. The static stress drops range from 0.1 and 136 MPa with a median value of 9.8 MPa (98 bars). The obtained seismic moments range from 7.49×10^{14} to 1.15×10^{18} Nm ($4.0 \leq M_w \leq 6.0$). The source radii are between 388 and 7073 m. we established a linear relationship between local and moment magnitudes. The scaling relations obtained indicated a slight deviation from self-similarity. High-stress drops observed in some events suggest elevated frictional strength and lower strain rates within faults, while lower stress drops may indicate general fault weakness. Although a definitive correlation between seismic moment and static stress drop was not observed universally, some events with lower seismic moment values also demonstrated lower stress drops. Furthermore, the corner frequency decreased with increasing seismic moment, with a slight depth dependence observed; shallower events tended to have higher corner frequency values than deeper ones. While there wasn't a clear depth dependence of stress drop values, a more pronounced depth dependence of seismic moment was observed, indicating that deeper events generally have larger seismic moment values in our study area. This implies that large earthquakes could still leave significant stress on faults, potentially leading to future events. The present study also reveals that M_w is lower than ML for all earthquakes with magnitudes > 4.0 . The coefficient of determination of the magnitude fit scale is found to be 0.91, which indicates the fit is good. Therefore, it is concluded that the newly derived magnitude scale is more consistent than the currently used ML scale for the study region.

Keywords

Northwest Himalaya, Seismicity, Stress Drop, Earthquake Scaling, Seismic Hazard

*Corresponding author: go2sanjay_p@yahoo.com (Sanjay Kumar Prajapati)

Received: 13 February 2025; **Accepted:** 28 February 2025; **Published:** 21 March 2025



Copyright: © The Author(s), 2025. Published by Science Publishing Group. This is an **Open Access** article, distributed under the terms of the Creative Commons Attribution 4.0 License (<http://creativecommons.org/licenses/by/4.0/>), which permits unrestricted use, distribution and reproduction in any medium, provided the original work is properly cited.

1. Introduction

Determining essential source characteristics such as seismic moment, stress drop, and source size accurately through field observation presents substantial hurdles in earthquake analysis. A comprehensive understanding of earthquake physics necessitates a meticulous analysis of these source parameters. Nevertheless, given the limited occurrence of major earthquakes, focusing on the significance of small and moderate earthquakes is crucial for understanding the underlying physics of earthquake sources. Understanding the relationships between the source factors of minor to moderate earthquakes is critical for learning valuable insights into the earthquake's origin. Several investigations have revealed that minor earthquakes contribute relatively little to the seismic moment released [15, 56]. Few studies have shown that smaller ruptures generated by minor earthquakes can cause as much tension as big faults [27]. However, because of the continent's high overall stiffness and the slowness of strain changes transmitted to the subcontinent, locating such modest-magnitude earthquakes is difficult [23]. Spectral methods serve as indispensable tools for earthquake analysis, offering valuable insights into seismic source parameters even when direct observation is impractical. Within the extensive literature on this subject, a multitude of studies have contributed diverse methodologies and theoretical frameworks [18-20, 58, 51, 67, 62, 4, 5, 73, 40, 9]. Their contributions span various aspects of seismic analysis, ranging from source modeling to parameter inference, enriching the field with diverse perspectives and methodologies. Despite the breadth of research across different seismic regions, particular attention has been directed towards the NW Himalaya region. Several studies have documented seismic investigations in this geologically complex area, shedding light on its seismic activity and associated source characteristics. Kumar (2008) and Kumar (2013) provided valuable insights into seismicity patterns and source parameters in the NW Himalaya region [43, 45]. Additionally, several authors have also contributed significantly to the understanding of seismic behaviour in this region [66, 49, 24]. These studies underscore the importance of continued research in this region to enhance our understanding of earthquake processes and improve seismic risk management strategies. The aim of our investigation was to examine the small to moderate earthquake's source parameters, occurring in the Northwest region. We employed the P and S wave spectra to compile data and discern meaningful correlations among these parameters. Additionally, we derived novel empirical relationships integrating the local magnitude ML with the seismic moment for enhanced analysis. We also attempted to obtain accurate estimates of stress release across a wide range of seismic moment values for a specific area. By applying scaling laws, we can make predictions about seismic hazards. Analysing small events enables the prediction of ground motion for more significant large earthquakes in the same area.

The study area and its adjoining regions is known for its high level of seismic activity and the potential for devastating earthquakes based on historical records. The region is known for its high seismic activity caused by the oblique compression between the Indian and Eurasian plates [65]. The study region is divided into six geographical regions: NW India, Pakistan, Nepal, Tibet, Kashmir, and Hindukush. The structural control of this area is determined by the presence of large, rigid lithospheric blocks. These blocks include the Indian plate in the south, the Afghan block in the southwest, the Turan plate in the west, and the Tarim block in the northeast. The current rate of relative plate motion between the Indian plate and the Eurasian plate, as determined by GPS data, is approximately 5.2 cm/year. [11, 21, 1]. The continuing compressional activity between the Indian and Eurasian plates renders the Himalayan area dynamically active in terms of deformation. This activity has resulted in a series of thrust faults, including the Main Frontal Thrust (MFT) in the south, the Main Boundary thrust (MBT) in the middle, and the Darvas-Karakul Fault and Gissal-Kokshal Fault in central Hindukush and Pamir [39, 70] (Figure 1). The region exhibits significant folding and thrusting, which commenced during the Cenozoic and Mesozoic eras, particularly in the Jurassic and Cretaceous periods. The tectonic regime can be divided into three main categories. First, there is the Himalayan collision zone, where the plates converge at a right angle. Second, there is the western syntaxis, which includes Pamir, Nanga Parbat, and the Kashmir-Hazara syntaxis. Lastly, there is the Western Fold Belt (WFB) of the Kirthar and Sulaiman ranges, which extends until the Chaman Fault, marking the western boundary of the Indian plate (Figure 1). The region is characterised by different tectonostratigraphic units, which are arranged from south to north. These units include the sub-Himalayan, Lesser Himalayan, Higher/Greater Himalayan, and Tethyan Himalayan zones. Various studies have provided valuable insights into these zones [53, 72].

The region experiences frequent seismic activity, with a range of earthquakes varying in magnitude from moderate to small. The region most affected by the M 7.8 great Kangra earthquake of 1905 experienced the biggest number of casualties, with over 1,900 deaths, and significant damage [48]. In 2005, a significant earthquake with a magnitude of 7.6, known as the Kashmir earthquake, caused extensive damage and resulted in over 80,000 casualties in the northwest limit of this region [46, 47]. The Himalayan region is experiencing the highest rate of convergence (12-16 mm/year) between the colliding plates, as detected using the global positioning system by [10]. The NW Himalaya experiences the highest level of seismic activity, but there is variance in seismicity along the 2,500 km extended Himalayan arc system from east to west. The majority of the high-magnitude earthquakes in the NW Himalaya region result in widespread destruction due to the thrust mechanism occurring along the major tectonic

zones. Nevertheless, the smaller earthquakes are causing other types of deformation, such as pure thrust/reverse, normal, and strike-slip. Most of these deformation patterns are oblique types, although they vary from place to place [44, 71]. In the current study area, the majority of small-scale earthquakes (Figure 1) are primarily characterised by thrust/reverse processes, together with a strike-slip component [71]. The seismological analysis of the region also indicates that the presence of earthquakes ($M_w > 4$) is strongly linked to both visible and hidden faults [38]. Seismic analysis mainly focuses on two regions: the Indus-Kohistan seismic zone (IKSZ) and the Hindu Kush seismic zone (HKSZ). The HKSZ is known for having earthquakes that occur at an intermediate depth of

300 km. The primary structural and tectonic features observed in the region and its surroundings include the major boundary thrust (MBT), Punjal Thrust (PT), Palampur Thrust (PMT), a portion of Jwalamukhi Thrust (JMT), minor lineaments, antiform, and neotectonic faults [61, 44] as illustrated in Figure 1. Our investigation successfully determines that certain areas are susceptible to significant earthquake hazards. The region has significant seismic activity, with earthquakes occurring at various depths ranging from shallow to intermediate. The region's stress and active deformation are evidenced by this. The intense subduction of the Eurasian and Indian continental lithosphere drives the seismic activity in the Pamir-Hindu Kush area.

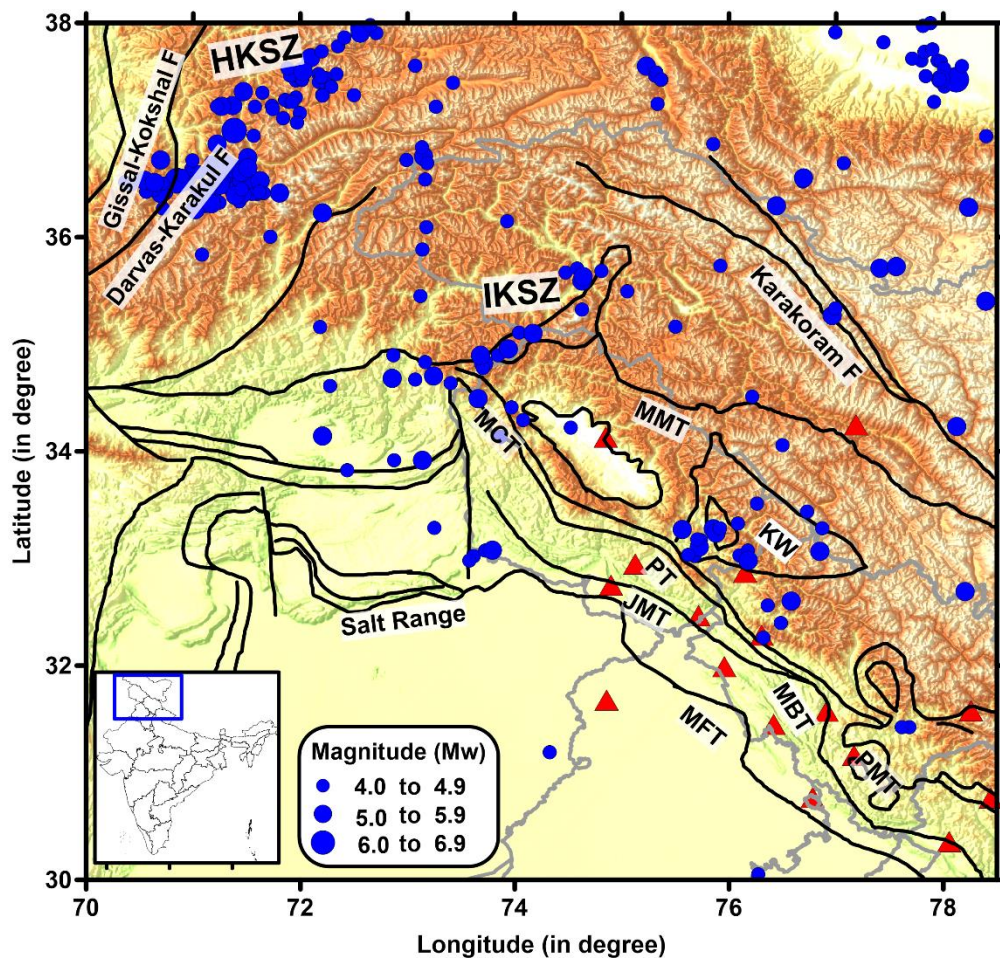


Figure 1. The tectonic map of the study area is overlaid onto a topographic map. Major tectonic fault lines in the study region are depicted in black, while India's political boundaries are shown in grey colour. Blue circles indicate earthquakes with magnitudes greater than 4.0 that occurred in the NW Himalayan region between 2013 and 2019. Red triangles are the location of permanent broadband seismological stations whose waveform data were utilized for the study. In the inset, a map displays the study area delineated by a blue rectangle. The expand form of the faults (MFT, MBT, MCT, PMT, PT, JMT, MMT, IKSZ and HKSZ) is mentioned in the manuscript.

2. Seismological Network and Data Analysis

The National Center for Seismology (NCS) operates a

seismic network throughout the Indian subcontinent region, consisting of 160 Broadband Seismic Stations (BBSs) and Strong Motion Accelerographs (SMAs) [12] (Figure 1, Inset). The seismological stations in the study region are equipped with 120-s broadband triaxial seismometers. These seismo-

meters are connected to 24-bit recorders with a VSAT hub, which allows for real-time data archiving. The recording equipment's instrumental response remains rather constant for ground velocities ranging from the seismometer's inherent frequency (0.0083 or 1 Hz) to around 25–50 Hz. The stations are situated on various geological formations, including alluvium, gneiss, and granite. Consequently, the impacts on the site can greatly differ from one station to another.

In the present study, earthquake data recorded at 15 broadband seismic stations from 2013 to 2019 were utilised to calculate the stress drop and establish a scaling relation. The arrival times of the P and S phases were determined using SEISAN, an earthquake analysis software. Time uncertainties were assigned to each phase, with a range of 0.05–0.30 s for P arrivals and 0.1–1.0 s for S arrivals for events within the network. Over a period of time Since 2013, NCS has documented approximately 10,000 earthquakes in the NW Himalayan region, spanning from 20–35 N and 72–90 E. Based on the error statistics, it is evident that the discrepancies in latitude, longitude, and depth are within a range of 5 km.

This study utilizes the velocity model developed by [43] for the Northwest Himalaya, which is derived from P- and S-wave arrival-time data and has an average V_p/V_s ratio of 1.73. We only considered earthquakes that were detected by at least a minimum of three stations, ensuring a good signal-to-noise ratio and precise location. The distances between the recording stations range from 10 to 500 km, while the

depth of the focal point spans from 0 to 200 km. Prior to selecting the amplitudes, the data underwent a process to eliminate the instrument response and were filtered within the frequency range of 1 to 10 Hz. The final dataset included 125 accurately located events that occurred between 2013 and 2019, with magnitudes ranging from 3.5 to 5.1. These events were used in the study region for stress drop analysis. The analysis has utilised the amplitude spectra of P waves (vertical component) and S waves (transverse component). To determine source parameters such as seismic moments (M_0), source dimensions (D), and stress drops (σ), as well as to establish regional scaling laws, a time window of 4 seconds has been selected to analyse the P waves considering their correlation with the earthquake's magnitude. All seismograms pertaining to the analyzed events underwent tapering using a Hanning window technique. Recorded by velocity seismographs, the seismograms were subjected to baseline correction through mean subtraction. Additionally, instrument response adjustments were implemented to convert all seismic recordings to displacement.

The Brune model was employed to accurately calibrate the observed P wave spectra, as illustrated in Figure 2. The determination of the window length for the S wave was guided by factors including the earthquake's magnitude and the distance from the seismic source. For S wave, window length was chosen as 10–20 s, depending on the magnitude and distance to the source (Figure 2).

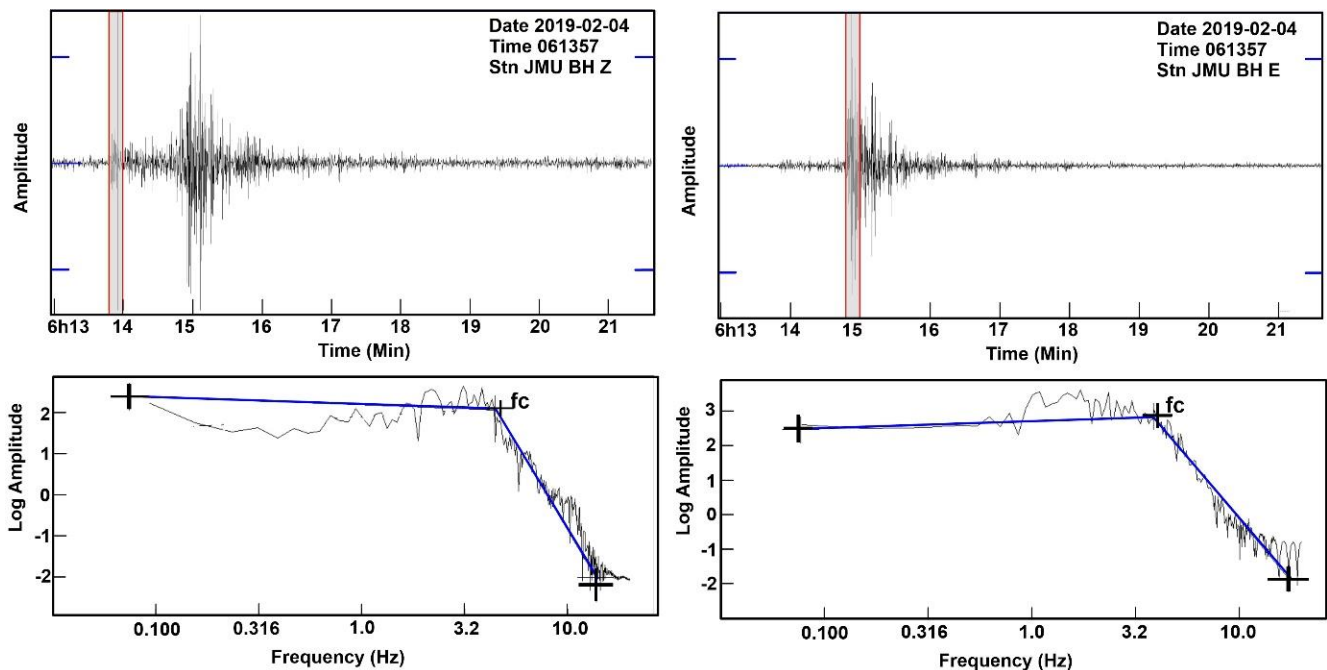


Figure 2. Waveform example of (a) P and (b) S waves. The lower part of the figure shows spectra and determined corner frequency (f_c).

Equation (1) describes the characteristics of the displacement amplitude spectrum.

$$U(f \cdot R) = G(R) \cdot S(f) \cdot A(f \cdot t). \quad (1)$$

where f represents the frequency, R denotes the hypocentral distance, $G(R)$ represents the attenuation caused by geometrical spreading, $S(f)$ represents the amplitude source spectrum, $A(f,t)$ represents the anelastic attenuation, and t represents the travel time. We applied correction techniques to the observed displacement spectrum ($U(f, R)$) to mitigate the adverse impacts of attenuation and geometrical spreading on amplitudes. This correction involved accounting for both attenuation, represented by $A(f,t)$, and geometrical spreading, denoted by $G(R)$. By applying these corrections, we aimed to ensure that the observed displacement spectrum accurately reflects the true seismic signal despite the effects of attenuation and geometrical spreading. Additionally, we successfully determined the source spectrum ($S(f)$) through our analysis.

According to the analysis undertaken, it has been established that all earthquakes being considered happened within a 300 km radius. Therefore, based on the research conducted by [30], the relationship $G(R) = 1/R$ was utilised to explain the decrease in intensity due to the dispersion of both P and S waves [31].

We then calculated the spectral source parameters, which are the moment magnitude (MW), stress drop ($\Delta\sigma$), seismic moment (M_0), corner frequency (f_c), and source radius (r). The analysis of the corrected source spectrum served as the foundation for these computations. The seismic moment was determined using the value of Ω_0 and applying the equation established by [37, 29, 15, 16, 41].

$$M_0(V_{PS}) = 4 \pi \rho R V_{P,S}^3 \frac{\Omega_0(P,S)}{kR(P,S)}. \quad (2)$$

The equation includes several parameters: ρ , which represents the average density ($\rho = 2.67 \text{ g/cm}^3$); $V(P, S)$ denotes the P and S wave velocities in the earthquake origin zone; R , which represents the hypocentral distance that causes the geometric spread; Ω_0 , the low-frequency spectral level; $R\theta\phi$, the average radiation pattern ($R\theta\phi = 0.52$ for P-wave and $R\theta\phi = 0.63$ for S-wave); and k represents the free surface amplification ($k = 2$).

The moment magnitude was calculated using the following equation proposed by [26]:

$$M_w = \left[\frac{2}{3} \log_{10}(M_0) \right] - 10.73. \quad (3)$$

The source radius and the stress drop have been calculated following equation [25]:

$$\Gamma = \frac{2.34V_p}{2\pi f_0} \quad (4)$$

Subsequently, the rupture area could be obtained as πr^2 . Further, the stress drops of the events were estimated utilizing the formulation as,

$$\Delta\sigma = 7/16 M_0/r^3 \quad (5)$$

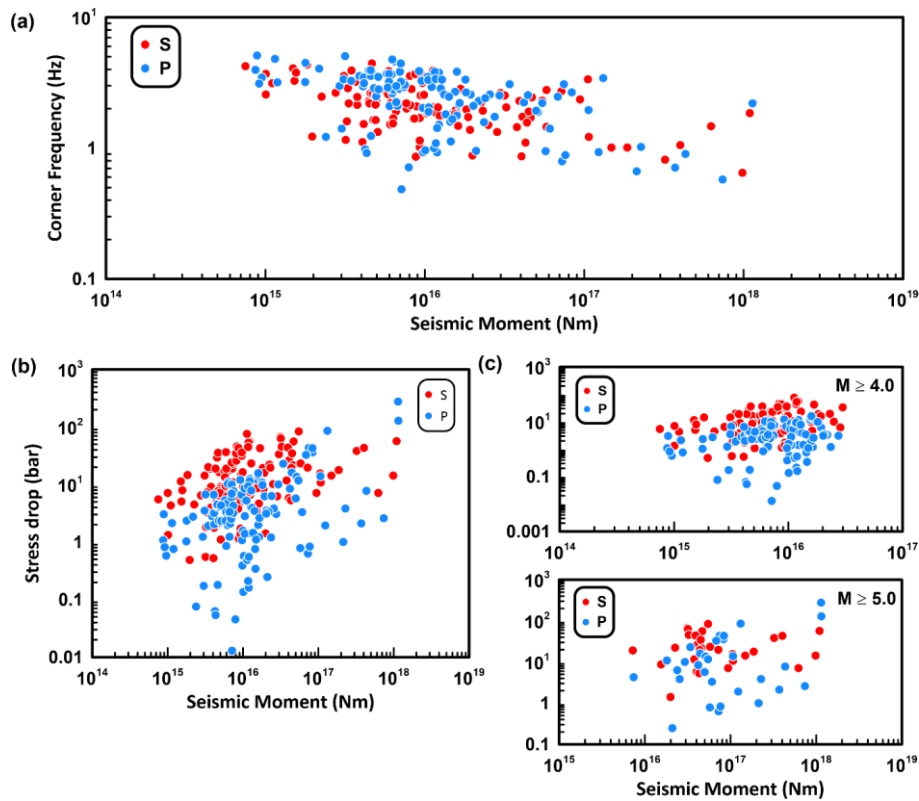


Figure 3. Relationship between (a) corner frequency and seismic moment and (b) stress drop and seismic moment determined from P (blue circles) and S (red circles) wave spectra (c) stress drop and seismic moment for the events with the magnitudes larger than 4.0 (upper) and 5.0 (lower).

3. Results and Discussion

The results derived from the displacement spectra analysis of both P waves and S waves are comprehensively summarized in [Tables 1 and 2](#), respectively. The calculated corner frequencies (f_c) from the Brune spectral model for all analyzed events range from 0.5 to 5.1 Hz for the P wave and from 0.6 to 4.5 Hz for the S wave. [Figure 3](#) depicts the relationship between corner frequency (f_c) and stress drop relative to seismic moment. [Figure 3a](#) illustrates the observed decrease in corner frequency (f_c) as the seismic moment (M_o) increases. Furthermore, it is noted that the corner frequency for P waves ($f_c(P)$) is higher than that for S waves ($f_c(S)$), with a $f_c(P)/f_c(S)$ ratio of 1.13. This finding is consistent with results reported in previous studies [[14](#), [2](#), [22](#), [54](#), [60](#), [8](#)], which reported similar ratios. Sivaram (2013) suggested that a lower ratio of $f_c(P)$ to $f_c(S)$ could stem from a non-double-couple source mechanism and/or a specific takeoff angle of observation [[59](#)]. They further concluded that scattering effects and insufficient sampling rate may lead to unsuccessful estimation

of f_c . However, our identified ratio of $f_c(P)$ to $f_c(S)$ closely corresponds to values reported in global stress drop studies conducted in collision and subduction environments, which typically exhibit very small ratios. The seismic moments derived from P waves ($M_o(P)$) span a range from 8.66×10^{14} Nm to 1.15×10^{18} Nm, while those obtained from S waves ($M_o(S)$) vary between 7.49×10^{14} Nm and 1.09×10^{18} Nm. The mean ratio between $M_o(P)$ and $M_o(S)$ is 1.23. This ratio is consistent with findings reported in several studies: Yang and Ben-Zion (2016) observed a ratio of 1.3 for small earthquakes in Turkey, Sile and Wder (2013) reported a ratio of 0.97 for earthquakes in Hungary, and Sivaram et al. (2013) found a ratio of 1.04 for events in the Kumaon region of the Himalayas [[71](#), [60](#), [59](#)]. Additionally, kumar (2014) documented a ratio of 1.11 for earthquakes in India, among other studies [[40](#)]. Furthermore, the P-wave source radii range from 606 to 7073 m, while the S-wave source radii vary from 388 to 3092 m. The mean ratio of P-wave source radii to S-wave source radii is 1.1. This value aligns with findings from multiple investigations conducted by [[22](#), [59](#), [60](#), [40](#), [8](#)].

Table 1. Spectral Source Parameter Analysis of P-Waves for the selected Seismic Events.

DATE & TIME	H (KM)	ML	f_c	Mw	M _o	r (m)	$\Delta\sigma$ (bar)	STN USE
20130115_203525	194	4.5	3.2	4.5	5.97E+15	951.1949	3.3	3
20130205_181747	202	4.6	2.1	4.5	6.75E+15	1580.941	2.1	3
20130217_013406	95	4.6	1.9	4.5	1.02E+16	1999.738	0.6	3
20130303_031227	10	5	1	4.8	2.10E+16	3417.903	0.2	4
20130430_094045	16	4.6	2.9	4.4	4.80E+15	1101.013	2.4	3
20130501_091946	16	4.6	1.5	4.5	1.23E+16	2625.332	1.4	3
20130520_171810	205	4.8	2	4.6	9.73E+15	1776.356	1.1	4
20130604_173445	14	4.9	2.1	4.8	2.02E+16	1465.898	3.1	4
20130629_031652	35	4.6	3.5	4.4	5.11E+15	976.6876	4.3	3
20130802_023237	17	5.3	0.9	5.2	7.63E+16	3428.675	0.8	4
20130802_213744	26	5.2	0.8	5.2	7.25E+16	4746.119	0.6	5
20130805_135744	16	4.2	1.4	4.1	3.01E+15	3910.326	0.2	4
20131005_002602	101	4.9	1.8	4.7	1.59E+16	3949.838	2	3
20131020_194503	82	5.2	2.5	5	4.43E+16	1244.687	16.1	6
2014 12 18_121416	195	4.9	2.5	4.7	1.42E+16	1282.216	3.5	4
20140114_154014	97	5	2.5	4.9	2.94E+16	1366.97	10.1	6
20140115_154404	86	4.9	1.8	4.7	1.35E+16	2195.847	1.4	5
20140221_064603	30	4.6	2.8	4.5	6.92E+15	1065.7	2.5	4
20140328_102409	84	5.2	2.2	5.1	5.46E+16	1463.357	11.8	4
20140503_225000	114	4.6	2.9	4.5	5.85E+15	1049.326	2.3	3
20140613_133237	29	4.9	2.1	4.5	6.01E+15	1439.407	0.9	4

DATE & TIME	H (KM)	ML	fc	Mw	Mo	r (m)	$\Delta\sigma$ (bar)	STN USE
20140703_204008	85	4.8	1.6	4.6	1.44E+16	1903.307	0.8	3
20140711_041410	91	4.9	2.2	4.8	1.65E+16	1430.005	2.6	5
20140719_071801	80	5.2	2	5.1	1.07E+17	1628.733	13.9	6
20140821_081119	15	4.8	1.7	4.7	2.75E+16	1877.113	3.1	7
20140917_061822	10	4.8	2.3	4.8	2.18E+16	1481.854	3.3	7
20140927_162240	26	4.6	1.9	4.6	1.06E+16	1630.12	1.4	4
20141023_040512	35	4.8	1.1	4.7	1.46E+16	2781.995	0.3	3
20141119_173001	100	5	3.2	4.5	7.38E+15	1034.083	4.3	3
20141205_161206	108	4.7	2.9	4.6	1.26E+16	1272.208	4	4
20150201_165445	200	4.5	3.4	4.3	3.09E+15	1080.469	3.5	3
20150321_174437	98	4.8	3	4.6	6.61E+15	1022.664	3.3	5
20150409_141216	10	4.6	3.5	4.4	1.04E+16	1072.297	5.3	4
20150530_164435	238	4.6	2.6	4.7	1.94E+16	1229.306	6.2	4
20150530_203620	92	5.4	2.5	5.2	6.83E+16	1472.572	32.9	6
20150601_222954	130	4.8	3.3	4.7	1.28E+16	1252.085	7.9	5
20150624_170959	113	4.5	3.8	4.5	6.98E+15	1004.665	6.1	3
20150629_220726	11	5.2	0.9	5.3	1.23E+17	3353.674	1.9	8
20150703_011312	17	4.6	0.9	4.6	1.20E+16	4463.769	0.2	7
20150703_011312	17	4.6	0.9	4.5	9.75E+15	4463.769	0.4	7
20150703_010746	19	6	0.6	5.8	7.40E+17	7073.353	2.6	8
20150703_031109	17	4.6	1	4.6	1.14E+16	3540.033	0.5	6
20150703_031725	10	4.5	1	4.5	1.01E+16	3178.582	0.1	6
20150714_143532	95	4.7	3.8	4.6	1.15E+16	854.712	9.2	4
20150714_143532	95	4.7	3.8	4.7	1.59E+16	854.712	15.8	4
20150810_100555	226	5.7	0.9	5.7	4.32E+17	4160.595	7.8	9
20150831_161341	132	4.7	2.8	4.5	6.36E+15	2877.59	2.8	4
20150901_191709	240	4.5	3.5	4.4	4.13E+15	936.0262	3.2	3
20151207_114752	10	4.9	2.1	4.8	2.05E+16	1528.294	3.6	3
20151207_151749	11	4.4	1.1	4.6	1.17E+16	3102.989	0.2	5
20151209_194015	10	4.1	1.2	4.2	2.39E+15	2539.235	0.1	5
20151213_200944	10	4.6	1.2	4.4	4.59E+15	2569.414	0.2	4
20160112_221257	35	4	4	3.9	8.66E+14	784.5624	1.1	3
20160123_045408	92	5	2.4	4.9	2.39E+16	1358.161	6.3	14
20160204_071206	20	4.3	3.2	4.1	1.19E+15	1163.654	0.8	4
20160206_215742	22	4.5	2.7	4.5	1.55E+16	1252.497	12.2	8
20160221_162538	88	4.2	4.5	4.1	1.78E+15	674.8172	2.4	4
20160229_182958	17	4	3.5	3.9	9.51E+14	972.2441	0.6	3
20160318_161007	10	5.2	3.1	5.1	7.46E+16	1013.451	43.4	9
20160401_212215	17	4.8	2	4.6	9.99E+15	1679.808	1.6	7

DATE & TIME	H (KM)	ML	fc	Mw	Mo	r (m)	$\Delta\sigma$ (bar)	STN USE
20160531_121021	96	4	4.8	4	1.14E+15	627.9518	2.1	3
20160610_230830	35	4.3	4	4.1	2.17E+15	778.9678	2.8	4
20160610_231117	111	4.7	3.8	4.6	1.23E+16	829.7783	11.4	10
20160629_090938	100	4	3.2	4.1	1.77E+15	980.5112	1	4
20160717_115225	35	4.5	5.1	3.8	8.85E+14	678.4897	3.1	12
20160726_215146	135	4.4	5	4.3	3.16E+15	606.3997	6.7	3
20160801_133806	20	4.5	3.7	4.3	4.68E+15	850.2689	4.6	8
20160827_011208	26	4.6	3	4.2	4.09E+15	1372.291	6.6	13
20160920_094203	100	4.5	3.7	4.4	5.95E+15	839.5596	4.6	11
20161217_172458	20	4.5	3.7	4.4	6.19E+15	831.5354	5	12
20170214_015200	146	4.6	2.9	4.6	1.11E+16	1150.052	5.3	14
20170228_134107	126	5.3	2.7	5.2	8.35E+16	1657.002	43.1	22
20170322_112618	11	4.9	1.6	4.8	2.35E+16	2382.253	1.2	19
20170708_101232	35	4.7	2.6	4.6	1.32E+16	1354.378	3.9	19
20170722_084533	264	4.6	2.2	4.5	1.63E+16	2117.762	1.2	5
20171019_011232	264	4.6	2.6	4.4	6.24E+15	1951.267	2	13
20171025_210216	41	4.5	3.3	4.6	1.05E+16	1007.751	8.6	9
20171107_141758	209	4.5	3.9	4.5	9.20E+15	794.0924	12	4
20171111_210018	106	4.8	3.4	4.7	1.17E+16	982.4678	9.3	13
20171206_232904	74	5.5	3.4	5.3	1.32E+17	989.3122	86	20
20171209_104351	10	4.6	3.9	4.5	1.59E+16	798.1909	14.5	4
20171229_145559	221	4.5	3.4	4.6	1.23E+16	966.5362	12.6	14
20180106_195512	10	4.5	3.1	4.4	9.12E+14	1059.728	0.8	6
20180109_000528	113	5	2.6	4.8	2.55E+16	1328.22	3.9	16
20180131_070836	193	5.9	2.2	5.8	1.15E+18	1426.149	128.5	6
20180228_164558	22	4.5	2.5	4.4	4.95E+15	1326.92	2.2	7
20180310_032134	16	4.5	2.8	4.4	5.13E+15	1315.012	2.3	9
20180315_145143	40	4.5	3.7	4.4	5.77E+15	873.8149	5.3	12
20180330_184616	238	5	3.1	4.9	3.40E+16	1031.619	23.1	16
20180424_155200	261	4.9	2.7	4.9	1.81E+16	739.3374	9.9	15
20180428_151345	88	5.2	1.9	5.1	5.12E+16	1936.178	13.7	17
20180502_225614	99	4.5	4.7	4.4	6.26E+15	638.3464	10.4	8
20180506_000113	89	5.3	2.6	5.1	8.31E+16	1526.885	36.1	12
20180509_104145	116	6.2	2.2	5.9	1.14E+18	2509.62	278.6	14
20180602_084540	10	4.7	2.1	4.6	1.06E+16	1902.583	2.8	10
20180614_101549	10	4.5	3.6	4.4	4.59E+15	910.6944	4.1	12
20180721_091931	40	4.5	2.8	4.4	6.15E+15	1191.788	2.5	8
20180803_002840	101	4.5	2.9	4.5	7.41E+15	1075.649	3.2	8
20180913_213109	230	4.5	3.3	4.6	9.55E+15	965.033	6.6	16

DATE & TIME	H (KM)	ML	fc	Mw	Mo	r (m)	$\Delta\sigma$ (bar)	STN USE
20181007_013550	119	4.5	4.6	4.4	6.40E+15	677.8837	11.1	9
20181007_135239	195	5	2.2	4.9	4.19E+16	1540.145	8.5	15
20181211_170404	165	4.6	3	4.5	7.49E+15	687.0376	7.7	8
20181217_010811	224	4.8	3.2	4.6	7.07E+15	680.3589	7	10
20181220_110812	13	5.2	1.4	5	6.08E+16	2667.724	3.3	10
20190122_002403	22	4.6	2.2	4.5	6.62E+15	1398.28	1.2	7
20190204_061225	125	4.5	3.9	4.4	4.46E+15	764.3784	4.4	12
20190204_061356	125	4.5	3.1	4.4	4.15E+15	962.3902	2	8
20190205_133832	30	4.5	3.3	4.3	3.45E+15	922.4255	1.9	6
20190205_164638	21	5.7	1	5.5	2.27E+17	2959.185	3.8	12
20190217_061528	96	5	3.4	4.8	1.80E+16	899.9542	10.8	8
20190217_225231	24	4.5	4	4.4	4.57E+15	762.5903	4.5	6
20190314_192540	115	4.7	4.4	4.5	7.06E+15	678.8595	9.9	8
20190612_030937	13	5.2	0.9	5.1	5.73E+16	3174.95	0.8	4
20190616_123904	31	4.6	0.9	4.4	4.32E+15	3281.185	0.1	3
20190908_022950	10	4.8	1.4	4.7	1.19E+16	2117.563	0.5	3
20190909_063800	44	4.9	1.7	4.7	1.49E+16	1808.161	1.1	3
20190924_110007	10	5.8	0.7	5.7	3.71E+17	4245.347	2.1	7
20191003_220115	197	4.5	3	4.3	2.91E+15	1012.17	1.2	13
20191009_104447	203	5.2	1.9	5.1	4.99E+16	1561.377	5.7	4
20191013_010010	222	4.5	3.6	4.4	3.88E+15	847.66	2.8	6
20191230_171636	10	4.6	0.5	4.5	7.12E+15	6230.184	0	7
20191230_171857	14	5.6	0.7	5.5	2.13E+17	4524.924	1	15
20191230_172017	10	4.8	0.7	4.6	7.91E+15	4235.522	0	15
20191230_172825	10	4.5	1	4.4	4.22E+15	3084.502	0.1	5

Table 2. Spectral Source Parameter Analysis of S-Waves for the selected Seismic Events.

DATE & TIME	H (KM)	ML	fc	Mw	Mo	r	$\Delta\sigma$ (MPa)	STN USE
20130115_203525	194	4.5	2.152	4.4	4.91E+15	84206.28	5.4	3
20130205_181747	202	4.6	1.647	4.4	4.75E+15	111213.1	2.1	3
20130217_013406	95	4.6	1.691	4.4	6.32E+15	141899.1	2	3
20130303_031227	10	5	0.878	4.8	1.99E+16	225373.8	1.4	4
20130430_094045	16	4.6	2.401	4.4	4.83E+15	74043.45	8.4	3
20130501_091946	16	4.6	2.768	4.4	5.64E+15	65285	16.9	3
20130520_171810	205	4.8	1.957	4.7	1.56E+16	91974.49	10	4
20130604_173445	14	4.9	2.637	4.8	2.99E+16	78800.48	33.6	4
20130629_031652	35	4.6	3.143	4.5	9.64E+15	58213.72	31.5	3

DATE & TIME	H (KM)	ML	fc	Mw	Mo	r	$\Delta\sigma$ (MPa)	STN USE
20130802_023237	17	5.3	1.457	5.1	5.79E+16	129746.1	23.3	4
20130802_213744	26	5.2	1.568	5	4.38E+16	170839.8	19.4	5
20130805_135744	16	4.2	1.604	4.2	3.24E+15	159324.4	1.8	4
20131005_002602	101	4.9	1.379	4.8	1.92E+16	219680.7	15.9	3
20131020_194503	82	5.2	2.787	5	5.79E+16	75292.82	23.4	6
20140114_154014	97	5	2.527	4.9	3.17E+16	73893.3	63.6	6
20140115_154404	86	4.9	1.701	4.6	9.28E+15	107728.7	4.9	5
20140221_064603	30	4.6	3.195	4.5	5.99E+15	53525.13	18.9	4
20140328_102409	84	5.2	1.9	5	4.48E+16	101189.4	35	4
20140503_225000	114	4.6	3.68	4.5	8.68E+15	47591.74	43.2	3
20140613_133237	29	4.9	1.917	4.4	6.58E+15	90127.09	3.5	4
20140703_204008	85	4.8	1.483	4.7	1.62E+16	115862.1	4.7	3
20140711_041410	91	4.9	1.725	4.8	1.87E+16	101822.1	8.4	5
20140719_071801	80	5.2	1.71	5	4.61E+16	101172	21.6	6
20140821_081119	15	4.8	1.974	4.7	1.82E+16	93669.38	19.3	7
20140917_061822	10	4.8	1.771	4.6	1.24E+16	105796.1	7.4	7
20140927_162240	26	4.6	2.004	4.5	7.69E+15	85668.53	6.8	4
20141023_040512	35	4.8	1.144	4.6	9.27E+15	155543.1	1.4	3
20141119_173001	100	5	3.017	4.4	7.20E+15	62771.94	19	3
20141205_161206	108	4.7	2.55	4.6	9.89E+15	76516.74	16.4	4
20141207_114752	195	4.9	2.05	4.6	1.12E+16	84383.41	10.7	4
20150201_165445	200	4.5	2.455	4.3	3.77E+15	77234.61	9.1	3
20150321_174437	98	4.8	2.878	4.4	3.28E+15	58928.63	7.4	5
20150409_141216	10	4.6	2.659	4	2.75E+15	74548.18	6.5	4
20150530_164435	238	4.6	2.346	4.4	4.97E+15	78205.2	9.1	4
20150530_203620	92	5.4	2.361	5.2	9.40E+16	107770.3	7.2	6
20150601_222954	130	4.8	1.742	4.6	1.25E+16	99848.46	6.6	5
20150624_170959	113	4.5	3.572	4.3	3.10E+15	51931.44	14.3	3
20150629_220726	11	5.2	0.866	5	4.04E+16	227113.9	5.8	8
20150703_011312	17	4.6	1.014	4.5	9.30E+15	198076.9	1.7	7
20150703_011312	17	4.6	1.014	4.4	9.46E+15	198076.9	5.2	7
20150703_010746	19	6	0.647	5.8	9.82E+17	309258.9	14.3	8
20150703_031109	17	4.6	0.859	4.5	8.76E+15	258880.3	1.1	6
20150703_031725	10	4.5	1.114	4.3	4.05E+15	185145.8	0.5	6
20150714_143532	95	4.7	3.558	4.6	9.66E+15	50868.44	36.3	4
20150714_143532	95	4.7	3.558	4.5	8.05E+15	50868.44	34.9	4
20150810_100555	226	5.7	0.816	5.6	3.22E+17	247517	38.4	9
20150831_161341	132	4.7	2.146	4.5	7.24E+15	101062.9	10.9	4
20150901_191709	240	4.5	2.084	4.5	8.90E+15	82645	5.7	3

DATE & TIME	H (KM)	ML	fc	Mw	Mo	r	$\Delta\sigma$ (MPa)	STN USE
20151207_114752	10	4.9	1.931	4.8	2.31E+16	93482.16	19.6	3
20151207_151749	11	4.4	1.156	4.3	3.19E+15	190680.3	0.6	5
20151209_194015	10	4.1	1.224	4.1	1.96E+15	157720.7	0.5	5
20151213_200944	10	4.6	1.541	4.5	6.30E+15	113435	2.1	4
20160112_221257	35	4	3.126	3.9	1.10E+15	55141.67	4.3	3
20160123_045408	92	5	2.235	4.8	2.25E+16	85254.15	22.1	14
20160204_071206	20	4.3	2.571	4	1.01E+15	68776.91	1.3	4
20160206_215742	22	4.5	1.635	4.4	4.91E+15	115247.9	2.4	8
20160221_162538	88	4.2	4.066	4.1	1.49E+15	45018.42	11.4	4
20160229_182958	17	4	3.701	3.9	1.00E+15	53697.2	7.1	3
20160318_161007	10	5.2	2.45	5	4.69E+16	72569.8	56.1	9
20160401_212215	17	4.8	2.115	4.4	6.21E+15	100660.4	8	7
20160531_121021	96	4	4.343	3.9	1.83E+15	38837.94	14.6	3
20160610_230830	35	4.3	2.471	4.2	2.25E+15	74053.82	4.5	4
20160610_231117	111	4.7	3.731	4.6	1.18E+16	46941.33	53.4	10
20160629_090938	100	4	3.263	4	1.52E+15	54036.92	5.1	4
20160717_115225	35	4.5	4.238	3.7	7.49E+14	43577.43	5.5	12
20160726_215146	135	4.4	3.775	4.1	1.56E+15	44952.37	8	3
20160801_133806	20	4.5	4.057	4.3	4.61E+15	43160.85	33.3	8
20160827_011208	26	4.6	3.219	4	3.68E+15	61803.96	18.9	13
20160920_094203	100	4.5	3.504	4.4	4.32E+15	50190.78	19	11
20161217_172458	20	4.5	3.928	4.3	3.46E+15	44200.17	20.1	12
20170214_015200	146	4.6	2.532	4.5	9.40E+15	71980.8	15.2	14
20170228_134107	126	5.3	2.313	5.1	5.46E+16	104937.1	83.9	22
20170322_112618	11	4.9	1.33	4.8	2.84E+16	150180.4	6.2	19
20170708_101232	35	4.7	1.883	4.6	1.16E+16	99792.95	10.7	19
20170722_084533	264	4.6	1.868	4.4	1.52E+16	132945.4	3.4	5
20171019_011232	264	4.6	2.2	4.5	6.77E+15	94074.63	8.2	13
20171025_210216	41	4.5	2.135	4.5	8.11E+15	86807.19	26	9
20171107_141758	209	4.5	3.422	4.6	1.17E+16	50873.5	45	4
20171111_210018	106	4.8	2.844	4.7	1.67E+16	62100.23	42.7	13
20171206_232904	74	5.5	3.356	5.2	1.06E+17	53899.4	15.6	20
20171209_104351	10	4.6	3.356	4.5	1.22E+16	50909.48	55.6	4
20171229_145559	221	4.5	2.824	4.4	8.26E+15	66739.39	46	14
20180106_195512	10	4.5	2.136	4.3	3.76E+15	80236.43	4	6
20180109_000528	113	5	2.053	4.9	3.25E+16	100166.8	45.5	16
20180131_070836	193	5.9	1.474	5.8	6.24E+17	124823.9	7.1	6
20180228_164558	22	4.5	1.531	4.3	4.12E+15	121559.9	1.8	7
20180310_032134	16	4.5	2.735	4.4	6.46E+15	69880.66	17.5	9

DATE & TIME	H (KM)	ML	fc	Mw	Mo	r	$\Delta\sigma$ (MPa)	STN USE
20180315_145143	40	4.5	3.88	4.4	5.92E+15	45837.7	36.6	12
20180330_184616	238	5	2.485	4.9	3.12E+16	72548.06	67.7	16
20180424_155200	261	4.9	1.507	4.7	2.50E+16	117119.7	10.2	15
20180428_151345	88	5.2	1.445	4.9	3.78E+16	124934.8	11.7	17
20180502_225614	99	4.5	4.43	4.4	4.66E+15	38941.08	35.9	8
20180506_000113	89	5.3	2.728	5.1	7.20E+16	74352.53	19.8	12
20180509_104145	116	6.2	1.857	5.9	1.09E+18	153193.6	56.7	14
20180602_084540	10	4.7	1.984	4.6	1.00E+16	93183.85	9	10
20180614_101549	10	4.5	3.948	4.3	4.53E+15	45668.71	29.5	12
20180721_091931	40	4.5	2.902	4.4	4.83E+15	74059.8	16.5	8
20180803_002840	101	4.5	2.632	4.4	5.78E+15	66845.05	13.5	8
20180913_213109	230	4.5	3.05	4.5	7.05E+15	59599.23	24.2	16
20181007_013550	119	4.5	3.929	4.6	1.13E+16	46025.56	75.8	9
20181007_135239	195	5	1.741	4.9	4.09E+16	106258.6	26.4	15
20181211_170404	165	4.6	3.032	4.5	7.25E+15	59228.39	22.7	8
20181217_010811	224	4.8	2.697	4.6	1.29E+16	67562.58	23.2	10
20181220_110812	13	5.2	1.221	5.1	1.07E+17	181536	10.8	10
20190122_002403	22	4.6	1.517	4.4	6.06E+15	121260.5	2.3	7
20190204_061225	125	4.5	2.199	4.4	4.50E+15	761.8132	4.5	12
20190204_061356	125	4.5	2.503	4.4	4.90E+15	66928.78	7.1	8
20190205_133832	30	4.5	2.603	4.4	4.71E+15	64357.56	7.7	6
20190205_164638	21	5.7	1.009	5.5	1.86E+17	166028.5	17.8	12
20190217_061528	96	5	1.822	4.8	1.55E+16	91944.42	8.7	8
20190217_225231	24	4.5	2.282	4.4	4.45E+15	73410.49	4.9	6
20190314_192540	115	4.7	2.196	4.6	7.64E+15	76285.39	7.5	8
20190612_030937	13	5.2	2.293	5	3.91E+16	73058.32	43.9	4
20190616_123904	31	4.6	2.585	4.5	5.88E+15	64805.7	9.5	3
20190908_022950	10	4.8	1.854	4.6	1.02E+16	90357.46	6.1	3
20190909_063800	44	4.9	2.055	4.7	1.21E+16	81519.58	9.8	3
20190924_110007	10	5.8	1.053	5.7	4.01E+17	159090.9	43.6	7
20191003_220115	197	4.5	1.327	4.4	5.06E+15	126241.7	1.1	13
20191009_104447	203	5.2	1.102	5.1	4.29E+16	152017	5.3	4
20191013_010010	222	4.5	2.194	4.3	3.33E+15	76354.93	3.3	6
20191230_171636	10	4.6	2.209	4.5	6.12E+15	75836.45	6.1	7
20191230_171857	14	5.6	1.013	5.4	1.48E+17	165372.9	14.3	15
20191230_172017	10	4.8	1.684	4.6	8.56E+15	99479.05	3.8	15
20191230_172825	10	4.5	2.619	4.4	4.57E+15	63964.39	7.6	5

The static stress drop value is a significant source parameter that quantifies the reduction in stress following an earthquake, averaged throughout the fault or rupture surface area. The stress drop values for the P wave range from 0.01 to 278 MPa, with a median value of 3.2 MPa. For the S wave, the stress drops values range from 0.5 to 84 MPa, with a median value of 10.2 MPa. The median value of both P and S waves was determined to be 9.8 MPa. Multiple researchers [34, 6, 42, 68] have documented a wide range of stress drop values for minor events. Allmann (2009) provide an estimation of stress drop for global earthquakes with magnitudes ranging from MW 5.2 to 8.3 [6]. The estimated stress drop values range from 0.3 to 50 MPa and are independent of the seismic moment. Oth (2010) discovered a range of stress drop values between 0.1 and 100 MPa for crustal events with magnitudes ranging from 2.7 to 8.0 in Japan [50]. In their study, Wu (2017) examined the 2011 Mineral Virginia Earthquake and its aftershocks (with a magnitude of 2.5 or greater) and determined that the stress decreases ranged from 0.02 to 67 MPa, with a median value of 3 MPa [68]. According to [68], smaller earthquakes can occur in areas with high or low stress drop, resulting in bigger fluctuations in stress drop for smaller occurrences. Figure 3b again illustrates the correlation between earthquake moment and static stress drop. While there is no evident correlation between the seismic moment and the static stress reduction for moderate to large events, Figure 3c reveals a notable shift occurring at about magnitude 4. The stress drop values for occurrences with magnitudes less than 4 are

positively correlated with magnitude, as shown in Figure 3b. Several studies have demonstrated that stress drop exhibits a depth-dependent variation [32, 35, 13, 7, 5, 6, 28, 17, 33, 67]. Allmann (2007) proposed that this variation in shallow crustal stress drop is driven by depth-related changes in S-wave behavior, suggesting an interplay between seismic wave characteristics and stress release mechanisms [5]. In contrast, Bilek and Lay (1998) attributed these depth-dependent differences in stress drop to changes in the mechanical stiffness within subduction slabs, indicating that lithospheric material properties significantly influence stress release at varying depths [13]. Jin (2000) said that an increase in effective normal stress can lead to a variation in stress declines with depth [34]. Allmann (2007) conducted a study on stress drop changes in minor earthquakes near Parkfield, California [5]. Their findings suggested that they were unable to detect any rise in stress drop as the depth increased. Parolai (2007) conducted an analysis of 523 aftershocks following the 1999 Kocaeli earthquake [52]. Their findings indicated that there is a trend for the stress drop value to increase with the size of the aftershocks. It was also found that the correlation between stress drop and depth is significantly affected by the choice of the velocity model [5]. Wu (2017) conducted a study on the 2011 Mineral Virginia Earthquake and its aftershocks, concluding that there is no correlation between the depth and stress decreases [68]. Wu (2018) examined four generated earthquake series in Oklahoma, USA and found no discernible correlation with depth [69].

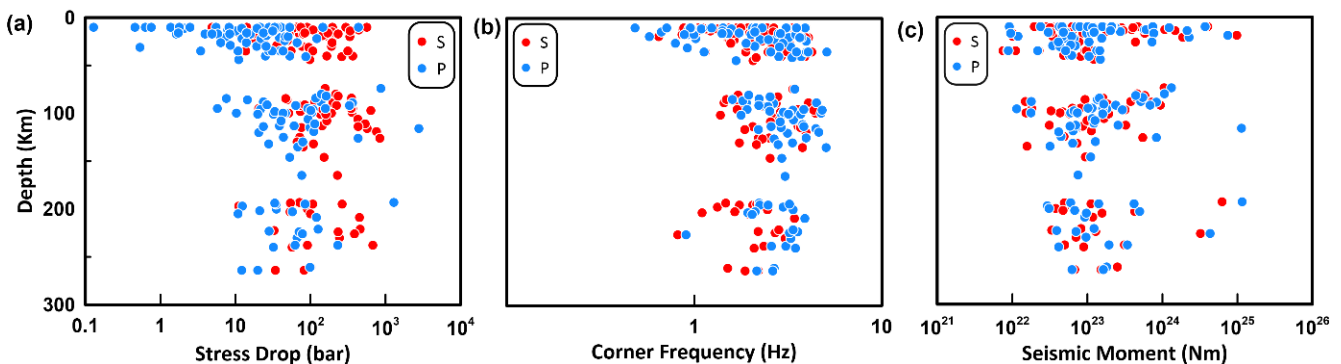


Figure 4. Depth dependence of (a) stress drop, (b) corner frequency, and (c) seismic moment determined from P (blue circles) and S (red circles) wave spectra.

Figures 4a, b, and c illustrate the correlation between the depth dependence of the static stress decrease, the corner frequency, and the seismic moment. Based on the data presented in Figure 4a, the static stress drop values exhibit a dispersed pattern, indicating that there is no discernible correlation between the stress drop values and depth. The corner frequency's depth dependency exhibits a similar behaviour, as shown in Figure 4b. Although there is no explicit correlation between depth and corner frequency values, it appears that events occurring at greater depths tend to have lower corner frequencies. The relationship between the seismic moment and depth is more evident compared to the stress drop and the corner frequency. Figure 4c illustrates that

certain events occurring at greater depths have higher seismic moment values. Figure 7 illustrates the correlation between seismic moment and corner frequency for the analyzed events. The constant Brune stress drop values are set at 0.1, 1, 10, and 100 MPa. Most events demonstrate self-similar scaling; however, stress drop values vary across different occurrences. The significant stress reductions observed during these episodes can be indicative of elevated frictional resistance and reduced fault deformation rates. Similarly, the low values of the stress drop can suggest an overall fragility of the faults in the studied area. The issue of magnitude saturation is significant as it pertains to the lack of saturation in various definitions of moment magnitude

[26], making it crucial in seismic hazard calculations. Abercrombie (2017) suggested that minimizing the uncertainty in stress drop estimates for these earthquakes could involve refining the selection of a source model based on either the shape of the observed spectral ratio or the P-to-S corner frequency ratios [3].

Various researchers have established correlations between local magnitude (M_L) and M_W to examine the region-specific relation between M_W and M_L [55, 36, 64]. Hence, it is crucial to discover empirical linkages that establish a connection with M_W . Figure 5 demonstrates the correlation between the moment magnitudes derived from the P and S wave displacement spectra and the local magnitude scale. However, Figure 5 shows that there is some scattering, particularly at small magnitudes. The origins of this scattering can be attributed to several adverse consequences observed in the calculation of local magnitude. M_L is determined by using either a Wood-Anderson (WA) seismograph or by simulating displacement seismograms using the Wood-Anderson seismo-

graph transfer function. However, there is uncertainty over the amplification of the Wood-Anderson seismographs. Uhrhammer and Collins (1990), Uhrhammer (1996) have stated that the usual WA seismograph has an effective amplification of approximately 2.080, as reported by [57, 63, 64]. Conversely, the natural frequency of the WA is 1.25 Hz. However, smaller earthquakes have a prominent frequency shift towards higher frequencies greater than 1.25 Hz. If the azimuthal distribution is disregarded or insufficient, the wave amplitudes are additionally influenced by rupture effects such as directivity. Moreover, the wave amplitudes and scattering may be influenced by the intricate nature of the source processes of the earthquakes being analysed and the site impacts. The presence of these effects is causing systematic inaccuracies in the estimations made by machine learning algorithms, which could potentially account for the scattered data points observed in Figure 5 at low magnitudes.

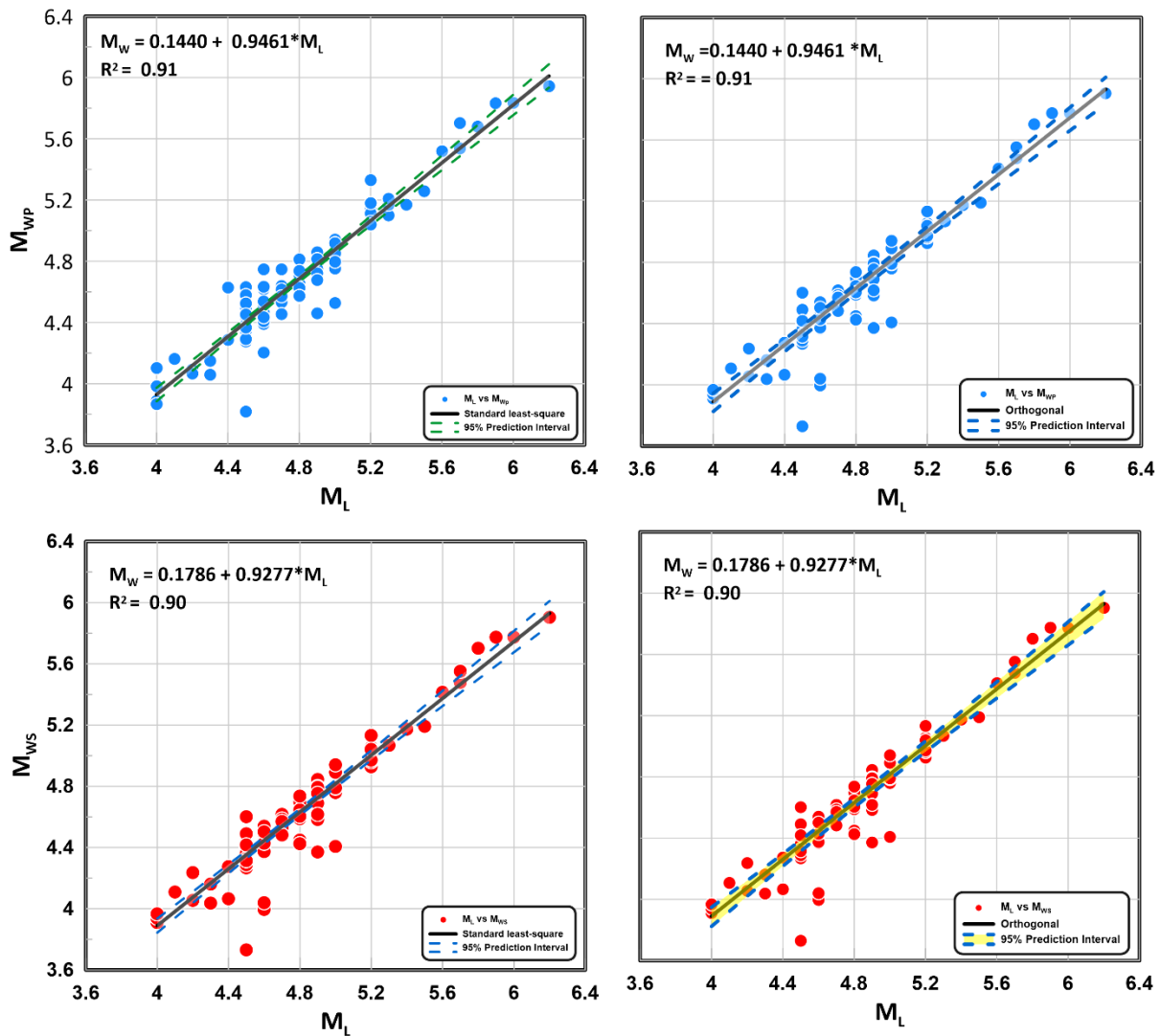


Figure 5. Comparison of orthogonal and standard least square regression analysis for determining M_W - M_L relationship. M_{WP} indicates the M_W magnitude obtained from P wave spectra, and M_{WS} indicates the M_W magnitude obtained from S wave spectra. R^2 indicates the correlation coefficient.

The least squares method is widely utilised in regression analysis. However, in this study, the magnitude scattering is a case that greatly affects the sensitivity of least squares estimates for regression models. Therefore, we conducted various types of regression analysis to accurately identify the magnitude of earthquakes. It is widely regarded as the most reliable option. We conducted tests on different methods of data analysis, including standard least-squares, robust

least-squares, and orthogonal regression. Each method aims to minimise the errors and provide the best fit to the data, either by minimising vertical offsets or perpendicular offsets to the best-fit line. The R^2 values obtained by two different methods are very close to each other. However, we found that the highest R^2 value was obtained from the standard least-squares regression analysis (Figure 5) as the MW-ML relationship.

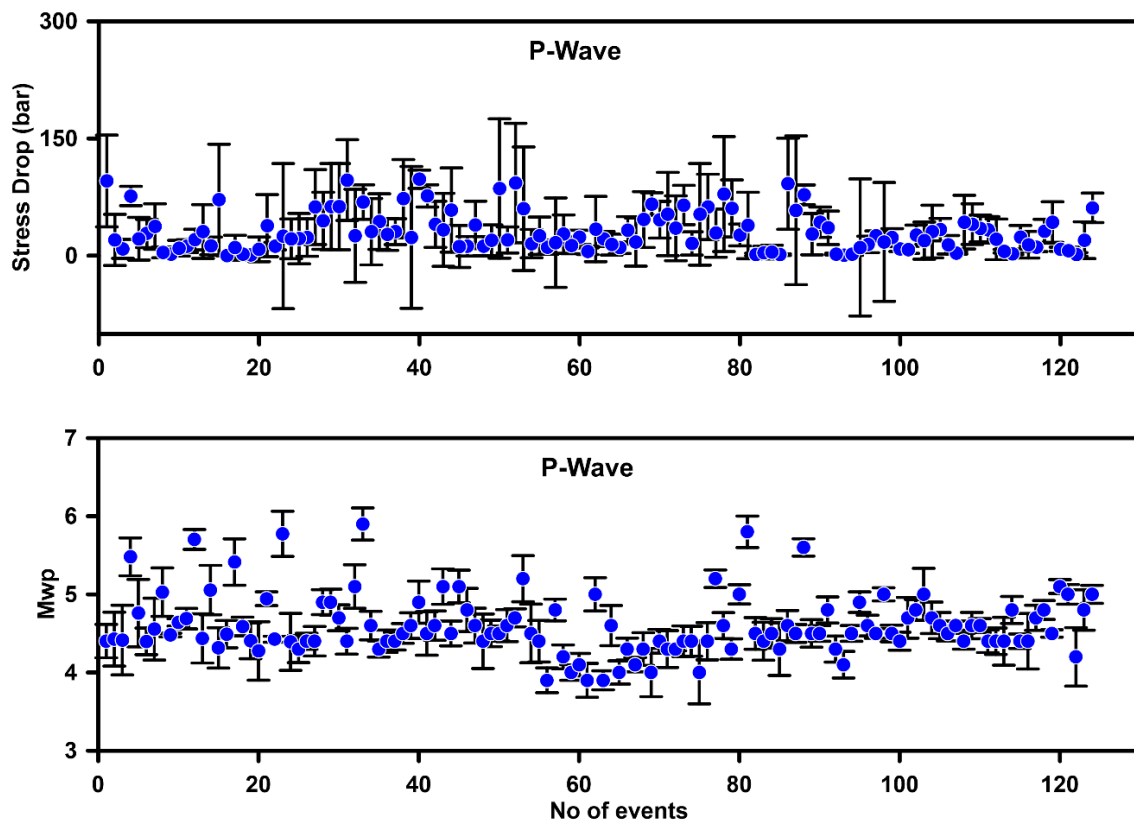
$$MW = 0.1440 (\pm 0.11) + 0.9461 (\pm 0.05) ML \text{ (for P wave)} \quad (6)$$

$$MW = 0.1786 (\pm 0.31) + 0.9277 (\pm 0.15) ML \text{ (for S wave)} \quad (7)$$

The current analysis reveals that there is a large fluctuation in the relationship between MW and ML, as well as its dependence on the zone in question, with an average error of approximately 0.08 magnitude units. However, because to the varied geology and geotectonic conditions that allow earthquakes to develop as a result of collisions, subduction, and complicated intra-plate tectonics, a single connection is not sufficient to scale the entire study region by itself.

In addition, the standard deviation for MW and $\Delta\sigma$ for each and every occurrence is presented in Figure 6. The small variation in Mw and $\Delta\sigma$ can be attributed to the nonlinear

behaviour of the P and S corner frequency and velocity model used for the computation of stress drop. The moment magnitude calculation that was performed in this investigation is presented in Table 3, together with the moment magnitude that was obtained by other seismological agencies (GCMT and ISC) was compared. It can be observed that the moment magnitudes that have been computed are, for the most part, compatible with the magnitudes that have been calculated by other agencies, particularly the relationship that has been acquired from the S wave spectra.



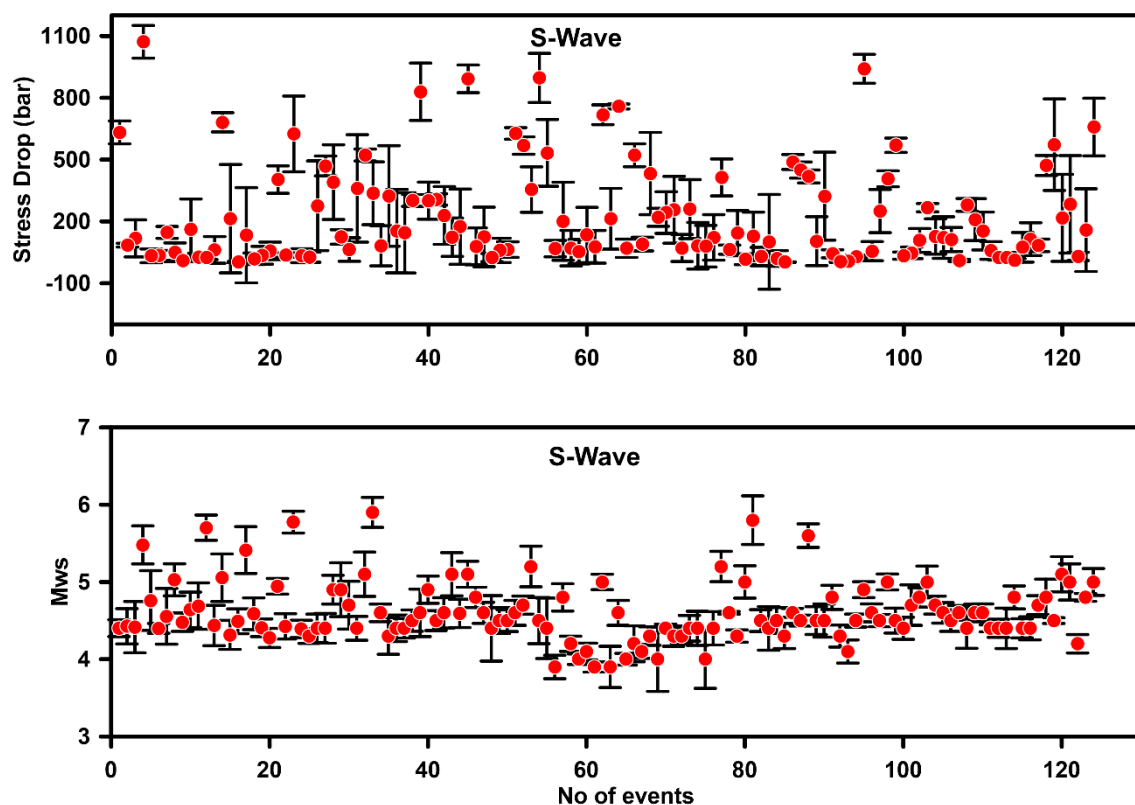


Figure 6. Standard deviation values for all calculated MW (P, S).

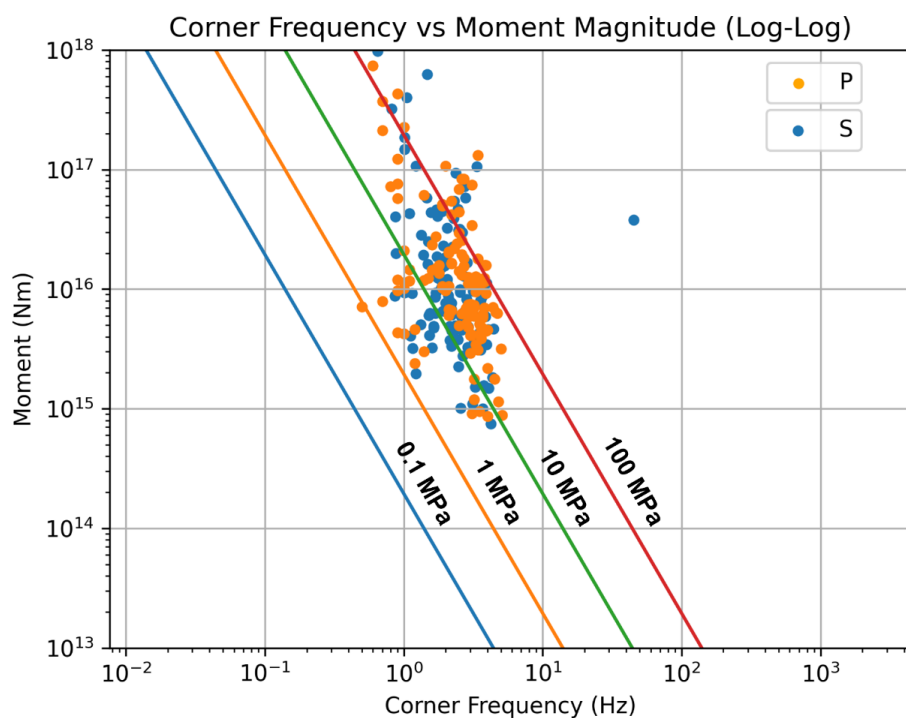


Figure 7. Seismic moment-corner frequency relationship for the analyzed events. Lines of constant indicate Brune stress drop 0.1, 1, 10 and 100 MPa.

Table 3. Comparison of calculated *M_w* in this study and by other agencies for the same earthquake.

Event Number	Local Magnitude by NCS	Present Study		<i>M_w</i>	
		<i>M_w</i> (S)	<i>M_w</i> (P)	GCMT	ISC
20130802_023237	5.3	5.1	5.2	5.1	5.1
20150530_203620	5.4	5.2	5.2	4.8	5.2
20150810_100555	5.7	5.6	5.7	5.9	5.9
20170228_134107	5.3	5.1	5.2	5.0	5.4
20171206_232904	5.5	5.2	5.3	5.2	5.2
20180131_070836	5.9	5.8	5.8	6.2	6.2
20180506_000113	5.3	5.1	5.1	5.0	5
20180509_104145	6.2	5.9	5.9	6.3	6.3
20190205_164638	5.7	5.5	5.5	5.3	5.3
20190924_110007	5.8	5.7	5.7	5.7	5.9
20191009_104447	5.2	5.1	5.1	5.0	5
20191230_171857	5.6	5.4	5.5	5.1	5.6

4. Conclusions

The current research aimed to elucidate the relationships between source parameters for 125 earthquakes occurring in the northwest Himalayan region, with local magnitudes between 4.0 and 6.0. We derived dynamic source parameters from the spectral analysis of P and S waves. Attenuation parameters for distance correction were obtained for low-frequency amplitude and corner frequency. Subsequently, seismic moment, moment magnitude, source radius, and stress drop were computed.

It has been observed that *f_c* is influenced by seismic moment, with *f_c* decreasing as the seismic moment increases, as anticipated. The ratio of P-wave velocity to S-wave velocity is determined to be 1.3. The seismic moment *M₀* and source radius *r* have a wide range of values, from 7.49 e14 to 1.15e18 Nm and 388–7073 m, respectively. The stress drop values $\Delta\sigma$ range from 0.1 to 136 MPa, with an average value of 9.8 MPa (98 bars). The high stress drops observed in these events suggest that the faults in the study area have high frictional strength and low strain rate. Additionally, the low value of the stress drop indicates a general weakness of the faults. There is no evident correlation between the seismic moment and the static stress drop. However, a significant shift occurs at around magnitude 4. The stress drop values for events with magnitudes smaller than 4 (ranging from 4.0 to 5.0) show a consistent increase as the magnitude increases. In addition, no correlation has been observed between stress drop values and depth. Furthermore, there have been no observations of depth

dependence of corner frequency. A clearer understanding of the depth dependence of the seismic moment is evident. Our findings suggest that the events occurring at greater depths exhibit higher seismic moment values within the study area. Despite the occurrence of numerous small events, a clear correlation between local magnitude (ML) and moment magnitude (MW) has been established. The provided equations express the relationship between moment magnitude (MW) and local magnitude (ML) for seismic events, specifically for P and S wave spectra. In the case of P waves, the equation $MW = 0.1440(\pm 0.11) + 0.9461(\pm 0.05) ML$ indicates that MW can be calculated by multiplying the ML value by 0.9461 and adding 0.1440, with associated uncertainties provided for each coefficient. Similarly, for S waves, the equation $MW = 0.1786(\pm 0.31) + 0.9277(\pm 0.15) ML$ suggests a different relationship between MW and ML, again with uncertainties specified for each coefficient. These relationships have been derived based on empirical analysis and are validated by comparing the calculated MW values with those obtained from waveform inversion techniques. The agreement between the calculated MW values and those from CMT analysis provides confidence in the accuracy of the equations. Understanding these relationships is crucial for conducting seismic hazard studies in the study area. Using these equations, researchers and seismologists can estimate the moment magnitude of seismic events more accurately, even when ML values are available. This information is vital for assessing the potential seismic risk and implementing appropriate mitigation measures in earthquake-prone regions.

Abbreviations

GCMT	Global Centroid Moment Tensor
CMT	Centroid Moment Tensor
ISC	International Seismological Centre

Acknowledgments

The authors thank the Director of the National Center for Seismology, Ministry of Earth Science, for his kind encouragement and supporting seismological monitoring and research. Authors acknowledge with thanks many informal discussions with NCS Scientists, which provided deep insight into several aspects of active tectonics and geodynamics of the study region.

Author Contributions

Vedprakash Thakur: Data curation, Software, Methodology, Investigation

Sanjay Kumar Prajapati: Writing – original draft, Conceptualization, Supervision, Resources

Birendra Pratap: Writing – review & editing

Uma Shanker: Visualization, Validation and editing

Sudipto Bhattacharjee: Map preparation, Analysis of data

Conflicts of Interest

The authors declare no conflicts of interest.

References

- [1] Arora, B., R., Gahalaut, V. K., and Kumar, N., 2012. Structural control on along-strike variation in the seismicity of the northwest Himalaya. *J Asian Earth Sci* 57, 15–24. <https://doi.org/10.1016/j.jseaes.2012.06.001>
- [2] Abercrombie, R. E., 1995. Earthquake source scaling relationships from –1 to 5 ML using seismograms recorded at 2.5-km depth. *Journal of Geophysical Research: Solid Earth*, 100, 24015–24036. <https://doi.org/10.1029/95JB02397>
- [3] Abercrombie, R. E., Bannister, S. J., Ristau, and Doser, D., 2017. Variability of earthquake stress drop in a subduction setting, the Hikurangi Margin, New Zealand. *Geophysical Journal International*, 208, 306–320. <https://doi.org/10.1093/gji/ggw393>
- [4] Allen, T. I., Gibson, G., Brown, A., and Cull, J. P., 2004. Depth variation of seismic source scaling relations: implications for earthquake hazard in southeastern Australia. *Tectonophysics*, 390, 5–24. <https://doi.org/10.1016/j.tecto.2004.03.018>
- [5] Allmann, B. P., Shearer, P. M., 2007. Spatial and temporal stress drop variations in small earthquakes near Parkfield, California. *Journal of Geophysical Research*, 112, B04305. <https://doi.org/10.1029/2006JB004395>
- [6] Allmann, B. P., and Shearer, P. M., 2009. Global variations of stress drop for moderate to large earthquakes. *Journal of Geophysical Research*, 114, B01310, <https://doi.org/10.1029/2008JB005821>
- [7] Asano, K., Iwata, T., and Irikura, K., 2003. Source characteristics of shallow intraslab earthquakes derived from strong-motion simulations. *Earth Planets and Space*, 55, e5–e8. <https://doi.org/10.1186/BF03351744>
- [8] Ataeva, G., Shapira, A., and Hofstetter, A., 2015. Determination of source parameters for local and regional earthquakes in Israel. *Journal of Seismology*, 19, 389–401. <https://doi.org/10.1007/s10950-014-9472-x>
- [9] Baltay, A., Ide, S., Prieto, G., and Beroza, G., 2011. Variability in earthquake stress drop and apparent stress. *Geophysical Research Letters*, 38, L06303, <https://doi.org/10.1029/2011GL046698>
- [10] Banerjee, P., and Burgmann, R., 2002. Convergence across the northwest Himalaya from GPS measurements. *Geophysical Research Letters*, 29(13), 30–1–30–4. <https://doi.org/10.1029/2002GL015184>
- [11] Banerjee, P., Burgmann, R., Nagarajan, B., and Apel, E., 2008. Intraplate deformation of the Indian subcontinent. *Geophysical Research Letters*, 35, L18301, <https://doi.org/10.1029/2008GL035468>
- [12] Bansal, B. K., Pandey, A. P., Singh, A. P., Suresh, G., Singh, R. K., & Gautam, J. L. (2021). National seismological network in India for real - time earthquake monitoring. *Seismological Society of America*, 92(4), 2255–2269. <https://doi.org/10.1785/0220200327>
- [13] Bilek, S. L., and Lay, T., 1998. Variation of interplate fault zone properties with depth in the Japan subduction zone. *Science*, 281, 1175–1178. <https://doi.org/10.1126/science.281.5380.1175>
- [14] Boatwright, J., Fletcher, J. B., and Fumal, T. E., 1991. A general inversion scheme for source, site, and propagation characteristics using multiply recorded sets of moderate-sized earthquakes. *Bulletin of the Seismological Society of America*, 81, 1754–1782. <https://doi.org/10.1785/BSSA0810051754>
- [15] Brune, J. N., 1970. Tectonic stress and the spectra of seismic shear waves from earthquakes. *Journal of Geophysical Research*, 75(26), 4997–5009. <https://doi.org/10.1029/JB075i026p04997>
- [16] Brune, J. N., 1971. Correction to tectonic stress and the spectra of seismic shear waves from earthquakes. *Journal of Geophysical Research*, 76(20), 5002. <https://doi.org/10.1029/JB076i020p05002>
- [17] Candela, T., Renard, F., Bouchon, M., Schmittbuhl, J., and Brodsky, E. E., 2011. Stress drop during earthquakes: effect of fault roughness scaling. *Bulletin of the Seismological Society of America*, 101, 2369–2387. <https://doi.org/10.1785/0120100298>
- [18] Chen, S., and G. Atkinson., 2002. Global comparisons of earthquake source spectra. *Bull. Seism. Soc. Am.* 92, 885–895. <http://doi.org/10.1029/2006JB004395>

- [19] Franceschina, G., Kravanja, S., and Bressan, G., 2006. Source parameters and scaling relationships in the Friuli-Venezia Giulia (Northeastern Italy) region. *Physics of the Earth and Planetary Interiors*, 154, 148–167. <https://doi.org/10.1016/j.pepi.2005.09.004>
- [20] Frankel, A., 1981. Source parameters and scaling relationships of small earthquakes in the northeastern Caribbean. *Bulletin of the Seismological Society of America*, 71, 1173–1190. <https://doi.org/10.1785/BSSA0710041173>
- [21] Gahalaut, V. K., and Kundu, B., 2012. Possible influence of subducting ridges on the Himalayan arc and on the ruptures of great and major Himalayan earthquakes. *Gondwana Research*, 21(4), 1080–1088. <https://doi.org/10.1016/j.gr.2011.07.021>
- [22] Garcia, J. G., Romacho, M. D., and Jiménez, A., 2004. Determination of near-surface attenuation, with κ parameter, to obtain the seismic moment, stress drop, source dimension and seismic energy for microearthquakes in the Granada Basin (Southern Spain). *Physics of the Earth and Planetary Interiors*, 141, 9–26. <https://doi.org/10.1016/j.pepi.2003.08.006>
- [23] Johnston, A. C., 1996. Seismic moment assessment of earthquakes in stable continental regions—I. Instrumental seismicity. *Geophysical Journal International*, 124(2), 381–414. <https://doi.org/10.1111/j.1365-246X.1996.tb07028.x>
- [24] Hajra, S., Hazarika, D., Shukla, V., Kundu, A., and Pant, C. C., 2022. Stress dissipation and seismic potential in the central seismic gap of the north-west Himalaya. *Journal of Asian Earth Science*, 239, 105432. <https://doi.org/10.1016/j.jseaes.2022.105432>
- [25] Hanks, T. C., and Wyss, M., 1972. The use of body-wave spectra in the determination of seismic-source parameters. *Bulletin of the Seismological Society of America*, 62(2), 561–589. <https://doi.org/10.1785/BSSA0620020561>
- [26] Hanks, T. C., and Kanamori, H., 1979. A moment magnitude scale. *Journal of Geophysical Research: Solid Earth*, 84, 2348–2350. <https://doi.org/10.1029/JB084iB05p02348>
- [27] Hanks, T. C. and Johnston, A. C., 1992. Common features of the excitation and propagation of strong ground motion for North American earthquakes. *Bulletin of the Seismological Society of America*, 82(1), 1–23. <https://doi.org/10.1785/BSSA0820010001>
- [28] Hardebeck, J. L., and Aron, A., 2009. Earthquake stress drops and inferred fault strength on the Hayward fault, east San Francisco Bay, California. *Bulletin of the Seismological Society of America*, 99, 1801–1814. <https://doi.org/10.1785/0120080242>
- [29] Haskell, N. A., 1964. Total energy and energy spectral density of elastic wave radiation from propagating faults. *Bulletin of the Seismological Society of America*, 54, 1811–1841. <https://doi.org/10.1785/BSSA05406A1811>
- [30] Havskov, J. and Ottemoller, L., 2010. *Routine Data Processing in Earthquake Seismology*. Springer, Berlin, 352 p.
- [31] Horasan, G., Ayşe, K. O., Aysun, B. G., and Niyazi, T., 1998. S-wave attenuation in the Marmara Region, northwestern Turkey. *Geophysical Research Letters*, 25, 2733–2736. <https://doi.org/10.1029/98GL02042>
- [32] Huang, M-W., Wang, J-H., Hwang, R-D., and Chen, K-C., 2002. Estimates of source parameters of two large aftershocks of the 1999 Chi-Chi, Taiwan, earthquake in the Chia-Yi area. *Terrestrial Atmospheric and Oceanic Sciences*, 13(3), 299–312. <https://doi.org/10.3319/TAO.2002.13.3.299>
- [33] Huang, M. H., Fielding, E. J., Dickinson, H., Sun, J., Gonzalez-Ortega, J. A., Freed, A. M., and Bürgmann, R., 2017. Fault geometry inversion and slip distribution of the 2010 Mw 7.2 El Mayor-Cucapah earthquake from geodetic data. *Journal of Geophysical Research: Solid Earth*, 122, 607–621. <https://doi.org/10.1002/2016JB012858>
- [34] Jin, A., Moya, C. A., and Ando, M., 2000. Simultaneous determination of site responses and source parameters of small earthquakes along the Atotsugawa fault zone, central Japan. *Bulletin of the Seismological Society of America*, 90, 1430–1445. <https://doi.org/10.1785/0119990140>
- [35] Jones, L. E., and Helmberger, D. V., 1996. Seismicity and stress-drop in the Eastern Transverse Ranges, southern California. *Geophysical Research Letters*, 23, 233–236. <https://doi.org/10.1029/96GL00012>
- [36] Joshi, V., Chopra S., and Kumar, S., 2020. A local magnitude scale ML for the Saurashtra horst: An active intraplate region, Gujarat, India. *Journal of Earth System Science*, 129, 114. <https://doi.org/10.1007/s12040-020-1379-z>
- [37] Keilis-Borok, V. I., 1960. Investigation of the mechanism of earthquakes. *Soviet Research Geophysics (English translation)*, 4, 29.
- [38] Khwaja, A. and Monalisa, A., 2005. Seismic activity in the western extension of Salt Range. *Pak Journal of Meteorology*, 2(3), 35–47.
- [39] Koulakov, and Sobolev, 2006. A tomographic image of Indian lithosphere break-off beneath the Pamir-Hindukush region. *Geophysical Journal International*, 164, 425–440. <https://doi.org/10.1111/j.1365-246X.2005.02841.x>
- [40] Kumar, A., Gupta, S. C., Jindal, A. K., and Ghangas, V., 2014. Seismicity and source parameters of local earthquakes in Bilaspur region of Himachal Lesser Himalaya. *Arabian Journal of Geosciences*, 7, 2257–2267. <https://doi.org/10.1007/s12517-013-0929-y>
- [41] Kumar, A., Kumar, A., Mittal, H., Kumar, A., and Bhardwaj, R., 2012. Software to estimate earthquake spectral and source parameters. *International Journal of Geosciences*, 3, 1142–1149.
- [42] Kumar, A., Mitra, S., and Suresh, G., 2015. Seismotectonics of the eastern Himalayan and Indo-Burman plate boundary systems. *Tectonics*, 34, 2279–2295. <https://doi.org/10.1002/2015TC003979>
- [43] Kumar, D., Sriram, V., Sarkar, I., and Teotia, S. S., 2008. An estimate of a scaling law of seismic spectrum for earthquakes in Himalaya. *Indian Minerals*, 61, 62(3–4, 1–4), 83–92.
- [44] Kumar, N., Sharma, J., Arora, B. R., and Mukhopadhyay, S., 2009. Seismotectonic model of the Kangra–Chamba sector of NW Himalaya: constraints from joint hypocenter determination and focal mechanism. *Bulletin of the Seismological Society of America*, 99(1), <https://doi.org/doi:10.1785.0120080220>

- [45] Kumar, N., Yadav, D. K., Mondal, S. K., and Roy, P. N. S. 2013. Stress drop and its relation to tectonic and structural elements for the meizoseismal region of great 1905 Kangra earthquake of the NW Himalaya. *Natural Hazard*, 69, 2021–2038, <https://doi.org/10.1007/s11069-013-0793-9>
- [46] Mahajan A. K. Naresh Kumar and Arora B. R. 2006. Quick isoseismal map of 8th October, 2005 Kashmir Earthquake. *Current Science*, 91(3), 356–361
- [47] Mahmood, H., & Ingham, J. M. (2011). Seismic vulnerability assessment of Pakistan unreinforced masonry buildings at a national scale. *Seismological Research Letters*, 82(5), 676–685. <https://doi.org/10.1785/gssrl.82.5.676>
- [48] Middlemiss, C. S., 1910. The Kangra earthquake of 4th April 1905. *Memoirs of the Geological Survey of India*, 38, 409.
- [49] Mishra, O. P., Vandana, Kumar, V., and Gera, S. K., 2020. A new insight into seismic attenuation characteristics of North-west Himalaya and its surrounding region: Implications to structural heterogeneities and earthquake hazards. *Physics of the Earth and Planetary Interiors*, 106500, <https://doi.org/10.1016/j.pepi.2020.106500>
- [50] Oth, A., Bindi, D., Parolai, S., Di Giacomo, D., 2010 Earthquake scaling characteristics and the scale-(in) dependence of seismic energy to moment ratio: insights from KiK-net data in Japan. *Geophysical Research Letters*, 37, <https://doi.org/10.1029/2010GL044572>
- [51] Oye, V., Bungum, H., and Roth, M., 2005. Source parameters and scaling relations for mining-related seismicity within the Pyhasalmi ore mine, Finland. *Bulletin of the Seismological Society of America*, 95, 1011–1026. <https://doi.org/10.1785/0120040170>
- [52] Parolai, S., Bindi, D., Durukal, E., Grosser, H., and Milkereit, C., 2007. Source parameters and seismic moment-magnitude scaling for Northwestern Turkey. *Bulletin of the Seismological Society of America*, 97, 655–660.
- [53] Powell, C. M., and Conaghan, P. J. 1973. Plate tectonics and the Himalayas, *Earth and Planetary Science Letters*, 20, 1–12, [https://doi.org/10.1016/0012-821X\(73\)90134-9](https://doi.org/10.1016/0012-821X(73)90134-9)
- [54] Prieto, G. A., Shearer, P. M., Vernon, F. L., and Kilb, D., 2004. Earthquake source scaling and self-similarity estimation from stacking P and S spectra. *Journal of Geophysical Research: Solid Earth*, 109, <https://doi.org/10.1029/2004JB003084>
- [55] Ristau, J., Rogers, G. C., and Cassidy, J. F., 2003. Moment magnitude-local magnitude calibration for earthquakes off Canada's west Coast. *Bulletin of the Seismological Society of America*, 93, 2296 – 2300. <https://doi.org/10.1785/0120030035>
- [56] Scholz, C. H., and Patience A. Cowie., 1990. Determination of total strain from faulting using slip measurements. *Nature* 346, 837–839.
- [57] Scordilis, E. M., 2006. Empirical global relations converting MS and mb to moment magnitude. *Journal of Seismology*, 10, 225–236. <https://doi.org/10.1007/s10950-006-9012-4>
- [58] Sharma, M. L., Wason, H. R., 1994. Occurrence of low stress drop earthquakes in the Garwal Himalayan region. *Physics of the Earth and Planetary Interiors*, 85, 265–272. [https://doi.org/10.1016/0031-9201\(94\)90117-1](https://doi.org/10.1016/0031-9201(94)90117-1)
- [59] Sivaram, K., Kumar, D., Teotia, Rai, S. S., Prakasam, K. S., 2013. Source parameters and scaling relations for small earthquakes in Kumaon Himalaya, India. *Journal of Seismology*, 17, 579–592. <https://doi.org/10.1007/s10950-012-9339-y>
- [60] Süle, B., and Wöber, Z., 2013. Earthquake source parameters and scaling relationships in Hungary (central Pannonian basin). *Journal of Seismology*, 17, 507–521. <https://doi.org/10.1007/s10950-012-9334-3>
- [61] Thakur, V. C., 1998. Structure of the Chamba Nappe and position of the Main Central Thrust in Kashmir Himalaya. *Journal of Asian Earth Sciences*, 16, 269–282. [https://doi.org/10.1016/S0743-9547\(98\)00011-7](https://doi.org/10.1016/S0743-9547(98)00011-7)
- [62] Tusa, G., and Gresta, S., 2008. Frequency-dependent attenuation of P waves and estimation of earthquake source parameters in southeastern Sicily, Italy. *Bulletin of the Seismological Society of America*, 98, 2772–2794. <https://doi.org/10.1785/0120080105>
- [63] Uhrhammer, R. A., and Collins, E. R., 1990. Synthesis of Wood-Anderson seismograms from broadband digital records. *Bulletin of the Seismological Society of America*, 80, 702–716. <https://doi.org/10.1785/BSSA0800030702>
- [64] Uhrhammer, R. A., Loper, S. J., and Romanowicz, B., 1996. Determination of local magnitude using BDSN broadband records. *Bulletin of the Seismological Society of America*, 86, 1314–1330. <https://doi.org/10.1785/BSSA0860051314>
- [65] Valdiya, K. S., 1991. Quaternary tectonic history of northwest Himalaya. *Current Science*, 61, 664–668.
- [66] Vandana and Mishra, O. P., 2019. Source characteristics of the NW Himalaya and its adjoining region: Geodynamical implications. *Physics of the Earth and Planetary Interiors*, 294, 106. <https://doi.org/10.1016/j.pepi.2019.106277>
- [67] Wu, Z. L., Chen, Y. T., and Mozaffari, P., 1999. Scaling of stress drop and high-frequency fall-off of source spectra. *Acta Seismologica Sinica*, 12(5), 507–515.
- [68] Wu, Q., and Chapman, M., 2017. Stress-drop estimates and source scaling of the 2011 Mineral, Virginia, mainshock and aftershocks. *Bulletin of the Seismological Society of America*, 107, 2703–2720. <https://doi.org/10.1785/0120170098>
- [69] Wu, Q., Chapman, M., and Chen, X., 2018. Stress-drop variations of induced earthquakes in Oklahoma. *Bulletin of the Seismological Society of America*, 108, 1107–1123. <https://doi.org/10.1785/0120170335>
- [70] Yadav, D. K., Kumar, N., and Paul, A., 2009. Recent seismicity and stress pattern in NW Himalaya. *Himalayan Geology*, 30(2), 139–145.

- [71] Yang, W., and Ben-Zion, Y., 2016. Corner frequency ratios of P and S waves and strain drops of earthquakes recorded by a tight network around the Karadere segment of the North Anatolian Fault Zone: evidence for non-classical source processes. *Geophysical Journal International*, 205(1), 220–235. <https://doi.org/10.1093/gji/ggv560>
- [72] Yin, 2006. Cenozoic tectonic evolution of the Himalayan orogen as constrained by along-strike variation of structural geometry, exhumation history, and foreland sedimentation. *Earth-Science Review*, 76, 1-131, <https://doi.org/10.1016/j.earscirev.2005.05.004>
- [73] Zobin, V. M., and Havskov, J., 1995. Source spectral properties of small earthquakes in the northern North Sea. *Tectonophysics*, 248, 207–218. [https://doi.org/10.1016/0040-1951\(94\)00273-C](https://doi.org/10.1016/0040-1951(94)00273-C)